



Structural defects and electronic properties of the Cu-doped topological insulator Bi_2Se_3

Yi-Lin Wang,¹ Yong Xu,² Ye-Ping Jiang,^{1,2} Jun-Wei Liu,² Cui-Zu Chang,^{1,2} Mu Chen,^{1,2} Zhi Li,² Can-Li Song,^{1,2} Li-Li Wang,¹ Ke He,¹ Xi Chen,² Wen-Hui Duan,² Qi-Kun Xue,^{1,2,*} and Xu-Cun Ma^{1,*}

¹State Key Laboratory for Surface Physics, Institute of Physics, Chinese Academy of Sciences, Beijing 100190, China

²State Key Laboratory of Low-Dimensional Quantum Physics, Department of Physics, Tsinghua University, Beijing 100084, China

(Received 21 June 2011; revised manuscript received 30 June 2011; published 17 August 2011)

Motivated by the occurrence of superconductivity transition in Cu-doped topological insulator Bi_2Se_3 , we perform a combined study of low temperature scanning tunneling microscopy/spectroscopy and angle-resolved photoemission spectroscopy experiments and of *ab initio* density functional theory to clarify the doping nature of Cu atoms in Bi_2Se_3 films. By measuring the structural and electronic properties of the Cu-doped Bi_2Se_3 films at different doping temperatures, we find that Cu atoms behave as donors at intercalated and interstitial sites in Bi_2Se_3 films. Only the interstitial defect density plays an important role in the observation of Landau quantization of the topological surface states in Bi_2Se_3 .

DOI: [10.1103/PhysRevB.84.075335](https://doi.org/10.1103/PhysRevB.84.075335)

PACS number(s): 68.37.Ef, 73.20.At, 68.35.Dv, 71.55.Ht

I. INTRODUCTION

Topological insulators (TIs) can host many novel fundamental physical phenomena, such as Majorana fermions and magnetic monopole, and may find applications in low-power-dissipation spintronic devices.^{1,2} Recent theoretical prediction^{3,4} and experimental verification⁴⁻⁶ of three-dimensional strong TIs (Bi_2Se_3 , Bi_2Te_3 , and Sb_2Te_3) have greatly stimulated the research interests in TIs worldwide. Doped with Fe, Mn, and Cr, the bismuth-based TI compounds can exhibit other interesting physical properties, such as ferromagnetism,⁷ quantized anomalous Hall effect,⁸ and superconductivity in the Cu-intercalated Bi_2Se_3 with a transition temperature of $T_c = 3.8$ K,^{9,10} which stimulates people to search for a topological superconductor.^{11,12} The superconducting phase $\text{Cu}_x\text{Bi}_2\text{Se}_3$ occurs only in a small composition range. Interestingly, the carrier density in $\text{Cu}_x\text{Bi}_2\text{Se}_3$ is very low, and it does not increase linearly with the concentration of the intercalated Cu atoms. Therefore, a comprehensive understanding of the doping nature of Cu atoms and the structural properties of the Cu-doped Bi_2Se_3 is highly desirable.

In this study, we combine scanning tunneling microscopy/spectroscopy (STM/STS), angle-resolved photoemission spectroscopy (ARPES), and first-principles calculations to investigate the structural and electronic properties of the Cu-doped Bi_2Se_3 films. We find that at room temperature and below, the Cu atoms can either intercalate into the van der Waals gaps between the neighboring quintuple layers (QLs) or occupy the interstitial sites within a QL, both of which always lead to donor states. We also observe the Landau quantization of the topological surface states in Cu-doped Bi_2Se_3 films when the mean distance between two interstitial Cu defects is larger than the magnetic length.

II. METHODS

The Bi_2Se_3 films were grown on bilayer graphene on 6H-SiC(0001) by molecular beam epitaxy and characterized *in situ* by low temperature STM (Unisoku) and by room temperature ARPES (VG Scienta). The base pressure of the system is better than 1.0×10^{-10} torr. High-purity Bi (99.999%), Se (99.999%), and Cu (99.999%) were thermally evaporated from Knudsen

cells. The Bi_2Se_3 films were grown at a substrate temperature of 220 °C, and the source temperatures of Bi and Se are 450 °C and 116 °C, respectively. Details of the film growth have been described elsewhere.^{13,14} After growth of a 20 QL Bi_2Se_3 film, Cu atoms were deposited. The deposition flux rate was ~ 0.033 monolayer (ML) per minute, as calibrated by the Cu-induced Si(111)-(5 \times 5) reconstruction. Here, 1 ML is defined as the Se areal atomic density of 6.74×10^{14} atoms/cm² on the Bi_2Se_3 (111) surface. The ARPES data were collected by a Scienta SES-2002 analyzer with an unpolarized He-I α (21.21 eV) lamp. The STM measurement was performed at 4.8 K in the constant current mode using electrochemically etched polycrystalline W tips. The bias voltage was applied to the sample. The STS spectra were acquired using a standard lock-in technique.

First-principles calculations using a Vienna *ab initio* simulation package¹⁵ were performed to simulate the structural and electronic properties of Cu-doped Bi_2Se_3 . The simulations use the Perdew-Burke-Ernzerhof-generalized gradient approximation exchange-correlation functional,¹⁶ the projector augmented wave method,¹⁷ and plane wave basis with a cutoff of 240 eV. To simulate the Bi_2Se_3 surface [Fig. 1(a)], a slab of 10 atomic layers (2 QLs) was constructed using the experimental lattice constants $a = 4.14$ Å and $c = 28.64$ Å,¹⁸ which is periodically repeated in the z direction separated by 10 Å vacuum layers. The bottom six atomic layers were fixed during relaxation, so the distance between QLs was fixed to the experimental value. To model the Cu defects, a 4×4 surface unit cell and a Γ -centered $3 \times 3 \times 1$ k -point grid, together with a Gaussian smearing scheme (broadening of 0.05 eV), were used. Relaxations were done until the remaining forces were < 0.01 eV/Å in a non-spin-polarized manner and self-consistent calculations were performed in a spin-polarized manner. In addition, the diffusion of Cu in the Bi_2Se_3 surface, which is modeled by a slab of 1 QL (because of the computational limitation), was simulated using the nudged elastic band method.¹⁹

III. RESULTS AND DISCUSSION

Bi_2Se_3 has a rhombohedral structure with the space group D_{3d}^5 ($R\bar{3}m$) and five atoms in one unit cell, as shown in

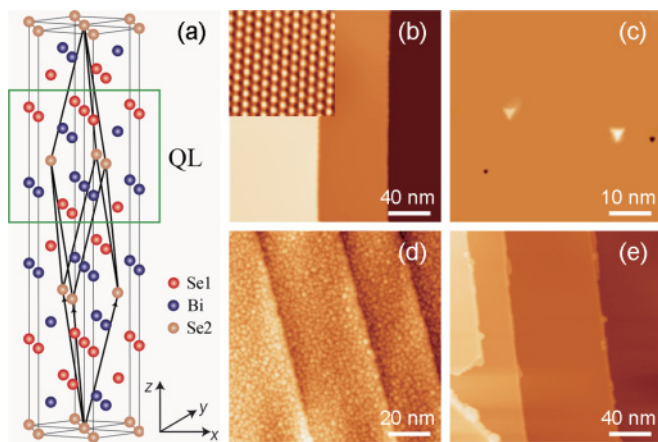


FIG. 1. (Color online) (a) Crystal structure of Bi_2Se_3 . The square outline (green line) indicates the Se-Bi-Se-Bi-Se QL. (b) STM image of the 20 QL Bi_2Se_3 film ($200 \times 200 \text{ nm}^2$, $V = 3 \text{ V}$). The inset shows the atomic-resolution image of the Bi_2Se_3 surface ($4 \times 4 \text{ nm}^2$, $V = -10 \text{ mV}$). Selenium atom spacing is $\sim 4.1 \text{ \AA}$. (c) STM image showing two dominant kinds of intrinsic defects on Bi_2Se_3 surface ($50 \times 50 \text{ nm}^2$, $V = 0.5 \text{ V}$). (d) and (e) STM images of the Bi_2Se_3 surface after deposition of 0.5 ML Cu at different substrate temperatures: (d) $T_{\text{sub}} = 100 \text{ K}$ ($100 \times 100 \text{ nm}^2$, $V = 3 \text{ V}$) and (e) $T_{\text{sub}} = 300 \text{ K}$ ($200 \times 200 \text{ nm}^2$, $V = 3 \text{ V}$). All STM images are obtained at the same tunneling current ($I = 0.1 \text{ nA}$).

Fig. 1(a). In the z direction, the atoms are arranged as a layered structure with hexagonal planes of Bi and Se, ... -Se1-Bi-Se2-Bi-Se1-Se1-..., where Se1 and Se2 denote the two inequivalent Se atoms in the crystal. The five individual atomic layers [within the square outline in Fig. 1(a)] form 1 QL. Within a QL, the chemical bond between Bi and Se atoms is of the covalent-ionic type, whereas between the adjacent QLs the interaction is of the van der Waals type.²⁰ Because of the unique bonding features of Bi_2Se_3 , high-quality films can be prepared by the van der Waals epitaxy method with a sharp interface on chemically inert substrate, such as graphene.^{14,21} Figure 1(b) shows a typical STM image of Bi_2Se_3 film with a thickness of 20 QLs grown on graphene formed on 6H-SiC(0001). The films grow in the z direction with a step height of a QL (0.95 nm). The inset of Fig. 1(b) shows an atomically resolved STM image of Bi_2Se_3 , which presents the hexagonal lattice structure of the Se-terminated (111) surface with the lattice constant $a = 0.41 \pm 0.01 \text{ nm}$. In contrast to the cleaved bulk single crystals, the density of intrinsic defects of our as-grown films is much lower; only few Bi_{Se} antisite defects (clover-shaped protrusions) and Se vacancies (triangular depressions) can be observed in Fig. 1(c). Such high-quality Bi_2Se_3 films enable us to more explicitly study the structural defects of Bi_2Se_3 after Cu doping.

Figure 1(d) and 1(e) shows the morphology of Bi_2Se_3 films after deposition of 0.5 ML Cu at 100 and 300 K, respectively. The 0.5 ML doping of Cu atoms is the maximum for studying the formation and property of individual defects in Bi_2Se_3 films, although it is much smaller than the minimum doping level ($0.10 \leq x \leq 0.30$) for $\text{Cu}_x\text{Bi}_2\text{Se}_3$ superconductivity. At 100 K the whole Bi_2Se_3 surface is covered by many small Cu clusters with a radius of $\sim 1.5 \text{ nm}$, whereas at 300 K the surface remains almost unchanged except for some

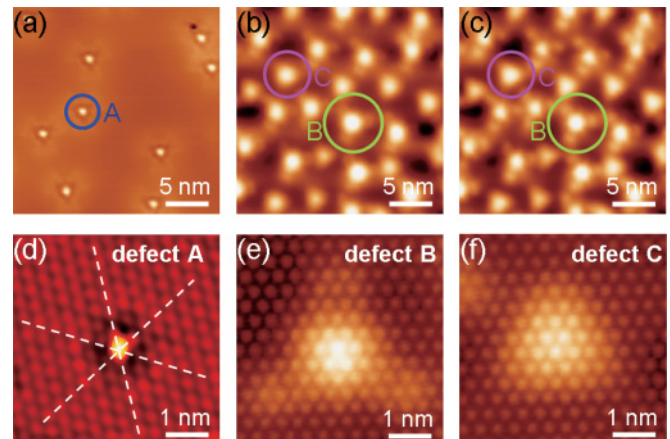


FIG. 2. (Color online) (a)–(c) STM images ($24 \times 24 \text{ nm}^2$) showing the surface structure of the Cu-doped Bi_2Se_3 films at different doping temperatures: (a) 100 K, 0.0017 ML ($V = 0.5 \text{ V}$, $I = 0.1 \text{ nA}$); (b) 300 K, 0.5 ML ($V = 0.5 \text{ V}$, $I = 0.1 \text{ nA}$); and (c) STM image of the same area in (b) at bias voltage $V = -0.5 \text{ V}$, $I = 0.1 \text{ nA}$. A, B, and C represents the three types of defects. (d)–(f) The atomic-resolution images ($5 \times 5 \text{ nm}^2$) of defects A, B, and C: (d) defect A ($V = 136 \text{ mV}$, $I = 0.7 \text{ nA}$), (e) defect B ($V = 1 \text{ mV}$, $I = 1.0 \text{ nA}$), and (f) defect C ($V = 1 \text{ mV}$, $I = 1.0 \text{ nA}$).

clusters at lower step edges. Detailed surface structures are shown in Fig. 2. The morphological difference between 100 and 300 K can simply be understood by a higher diffusion coefficient at a higher temperature. The diffusion coefficient D is expressed by the Arrhenius equation $D = D_0 \exp(-E/kT)$, where D_0 is a frequency factor, E is the activation energy for diffusion, k is the Boltzmann constant, and T is the temperature. For the simplest case, $D_0 = \nu a^2$, where ν is the vibration frequency ($\sim 10^{12} \text{ Hz}$) and a is the lattice constant. From our first-principles calculations, the activation energies for Cu atom diffusion in directions parallel and perpendicular to the surface are 0.317 and 0.944 eV, respectively. Because of the large layer spacing between adjacent QLs (the Se1-Se1 distance is 336 pm)²² and relatively weak electrostatic bonding forces, the diffusion barrier for Cu atoms in the van der Waals gaps is almost the same as that on the surface. The anisotropic diffusion originates from the layered structure, with a different bonding nature within and between QLs, and agrees well with the result of Cu diffusion in Bi_2Te_3 .²³ The calculated diffusion coefficients are $D_{\parallel} \approx 10^{-18} \text{ cm}^2/\text{sec}$ and $D_{\perp} \approx 10^{-50} \text{ cm}^2/\text{sec}$ at 100 K and $D_{\parallel} \approx 10^{-8} \text{ cm}^2/\text{sec}$ and $D_{\perp} \approx 10^{-18} \text{ cm}^2/\text{sec}$ at 300 K, respectively. This means that the diffusion of Cu atoms is nearly frozen so that clusters form on the surface at 100 K. At 300 K, Cu atoms can diffuse long enough to cross the terraces and intercalate into the van der Waals gaps before they meet and form clusters.

Careful STM observation reveals a very different surface structure of the Cu-doped Bi_2Se_3 films, depending on the substrate temperatures during Cu deposition (100 and 300 K). As shown in Fig. 2, three kinds of defects, labeled A, B, and C, are formed. They appear quite different from the intrinsic defects of Bi_2Se_3 [Fig. 1(c)]. At 100 K [Fig. 2(a)], defect A is imaged as a bright spot surrounded by a region of triangular depression. At 300 K [Fig. 2(b)], two defects (B and C) are observed that appear as bright triangular protrusions with a

spatial extension of ~ 4 nm. The contrast of defects B and C remains basically the same in both filled and empty states, as shown in Fig. 2(b) and 2(c), which were obtained from the same area.

Atomic resolution images are used to understand the structure of the Cu-induced defects. As shown in Fig. 2(d), defect A formed at 100 K is actually a single Cu atom adsorbed on the top site of a surface Se atom. As a scattering center, the Cu monomer can induce standing waves on the surface of Bi_2Se_3 (data not shown), indicating the impurity scattering potential is large. The Cu monomers can easily move on the surface by small perturbations induced by the tip during scanning; this is consistent with the small diffusion barrier on the surface. In the atomic resolution images of defects B and C (Fig. 2(e) and 2(f)), there is a common feature in that the surface lattice of the Se atoms is not disturbed compared to that of the clean surface, suggesting that the Cu atoms are located beneath the top Se plane. Each triangular defect should correspond to a Cu atom situated at the center of the defect underneath. The highest contrast of the triangular defects occurs at the position of the top Se atoms (defect B) or the positions of three adjacent Se atoms (defect C). We also deposited Cu atoms on the Bi_2Se_3 films at lower substrate temperatures (160 and 220 K); the resultant defects showed behavior similar to that of defects B and C.

Although the morphology of Bi_2Se_3 films after Cu deposition at 300 K does not change much compared to the bare film, the electronic properties of the Cu-doped Bi_2Se_3 surface are modified significantly. In STS, the dI/dV spectrum measures the local density of states of electrons. Figure 3(a) shows the dI/dV curves on the surface of pure Bi_2Se_3 (top) and Cu-doped Bi_2Se_3 (bottom). The minima (indicated by arrows) correspond to the Dirac points of the topological surface states of pure and Cu-doped Bi_2Se_3 films, which are located ~ 200 meV (top) and 350 meV (bottom) below the Fermi energy (E_F), respectively. The pure Bi_2Se_3 is n -type because of the presence of intrinsic Se vacancies. Upon Cu doping, a shift of the Dirac point (~ 150 meV) occurs, indicating that Cu atoms are electron donors. This behavior is also verified by the ARPES measurement. The band structure in the vicinity of the Γ point of the pure and Cu-doped Bi_2Se_3 is shown in Fig. 3(b). For pure Bi_2Se_3 , the Dirac point is located 145 meV below E_F and the conducting band is not observed, indicating the Bi_2Se_3

sample is a nearly intrinsic TI. The discrepancy in the position of the Dirac point measured by ARPES and STS probably results from surface charging in the STM measurement.¹³ For Cu-doped Bi_2Se_3 , the conduction band is clearly observed and the Dirac point is located 280 meV below E_F , which shifts by ~ 135 meV compared to that of pure Bi_2Se_3 . The result shows that the surface states of Cu-doped Bi_2Se_3 still exist and only undergo a rigid shift to lower binding energy. Thus, the Dirac point position relative to the bulk bands and the slope of the surface state do not change.

Based on the preceding experimental observations on Cu-doped Bi_2Se_3 films, we now discuss the positions of Cu atoms in Bi_2Se_3 . Unlike defect A, defects B and C are located below the top layer of the first QL. In terms of the tetradymite structure of Bi_2Se_3 , there are four possible sites the Cu atoms can occupy: (1) the Se lattice site, (2) the Bi lattice site, (3) the van der Waals gap between QLs, and (4) the interstitial sites in the first QL. Because of the different chemical properties of Cu and Se atoms, the substitution of Cu atoms for the Se sites is not likely.²⁴ If Cu atoms occupy the Bi lattice site, the resulting defects should exhibit a feature like that in Ca-doped Bi_2Se_3 ²⁵ and Mn-doped Bi_2Te_3 ⁷; however, the STM images (Fig. 2) of defects B and C do not show evidence for substituted Cu_{Bi} defects. Therefore, the first two candidates can be safely ruled out.

Because of the layered structure of Bi_2Se_3 and the diffusion of Cu atoms on the surface of Bi_2Se_3 , as discussed earlier, intercalation of Cu atoms into the van der Waals gaps is expected. Such a situation leads to donor states, which is consistent with our observation. On the other hand, within the covalently bonded QL, the Bi-Se distance is 284 and 304 pm for Bi-Se1 and Bi-Se2, respectively.²² The ionic radius of Cu is ~ 96 pm. Therefore, there is enough space between the Bi and the Se plane for the accommodation of interstitial Cu atoms. In this case, the Cu atom can lose one of its electrons and act as a donor. It is consistent with the n -type doping behavior of Bi_2Se_3 after Cu deposition. Figure 4 shows the theoretically calculated stable interstitial and intercalated sites for Cu atoms. There are two interstitial sites (marked (i) and (ii)) and three intercalated sites (marked (iii) through (v)). Our calculations indicate that the Cu atoms at intercalated sites are more stable than those at the interstitial sites; the largest energy difference is ~ 0.28 eV.

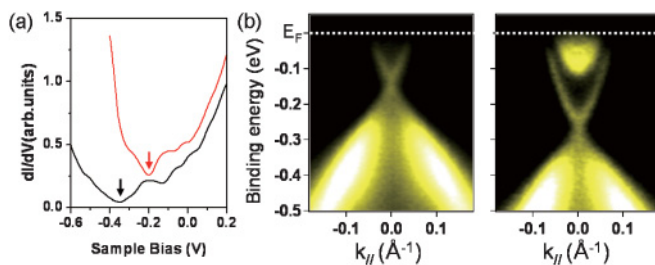


FIG. 3. (Color online) (a) dI/dV spectra taken on a pure Bi_2Se_3 surface (top, red) and a Cu-doped Bi_2Se_3 surface (bottom, black). The set point is $V = 0.2$ V, $I = 0.1$ nA. The arrows indicate the Dirac point. The curves are offset vertically for clarity. (b) ARPES spectra of pure Bi_2Se_3 (left) and Cu-doped Bi_2Se_3 (right) films measured in the Γ -K direction.

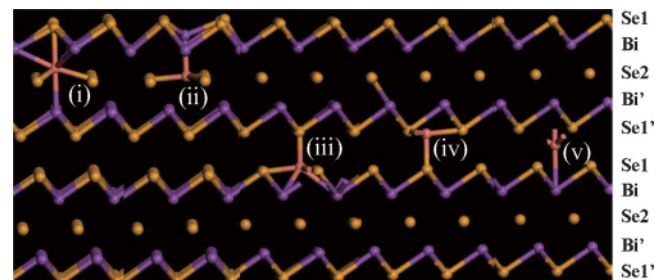


FIG. 4. (Color online) Interstitial and intercalated sites for Cu dopants. The interstitial sites are (i) below Se1, hollow Se2, 0.8 Å above Se2 and (ii) below Bi1, hollow Se2, 0.2 Å above Se2. The intercalated sites are (iii) below Se1', hollow Se1, 0.3 Å above Se1; (iv) hollow Se1', top Se1, 0.2 Å below Se1'; and (v) hollow Se1', top Bi1, 1.1 Å below Se1'.

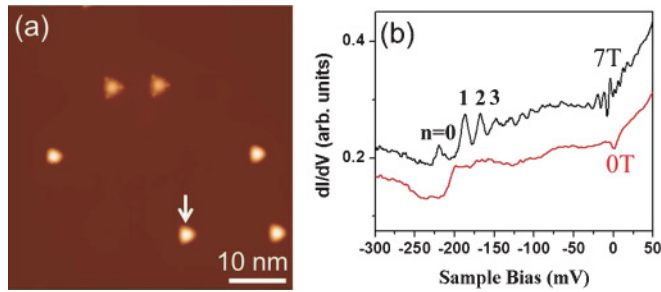


FIG. 5. (Color online) (a) STM image ($50 \times 50 \text{ nm}^2$, $V = 1.0 \text{ V}$, $I = 0.1 \text{ nA}$) of the Bi_2Se_3 surface after deposition of $\sim 0.05 \text{ ML}$ Cu at 300 K . (b) The dI/dV spectra on defect C (marked by an arrow in (a)) at 0 T (bottom, red) and 7 T (top, black) magnetic field. The set point is $V = 0.05 \text{ V}$, $I = 0.1 \text{ nA}$. The curves are offset vertically for clarity.

Because of the anisotropic diffusion behavior of Cu atoms in Bi_2Se_3 , most Cu atoms form intercalated defects and a few form interstitial defects. The total number of defects B and C is much smaller than the expected number of Cu atoms and reaches a saturation level after $\sim 1 \text{ ML}$ Cu deposition. According to the defect center position, defects B and C are ascribed to the Cu atoms located at interstitial sites (i) and (ii), respectively. The intercalated Cu atoms are not imaged directly.

A TI has a metallic surface state, which can be quantized into Landau levels (LLs) when a perpendicular magnetic field is applied.^{13,26} Because of the two-dimensional nature of the quantized states, the LLs are suppressed by defect scattering. When the distance between defects is comparable to or smaller than the magnetic length, the LLs are strongly suppressed and eventually disappear.¹³ We then studied the influence of interstitial and intercalated Cu defects on Landau quantization of surface states of Bi_2Se_3 films. Figure 5(a) shows the surface structure of a 20 QL Bi_2Se_3 film after deposition of $\sim 0.05 \text{ ML}$ Cu. Assuming the Cu atoms are evenly distributed in the film (considering the diffusion of Cu atoms from surface to bottom, the Cu defect density in the surface should be larger, although our assumption does not influence the conclusion), the total interstitial and intercalated Cu defect density is $1.69 \text{ defects}/100 \text{ nm}^2$. As shown in Fig. 5(a), the observed interstitial defect density is $\sim 0.24 \text{ defects}/100 \text{ nm}^2$; therefore, the intercalated defect density is $\sim 1.45 \text{ defects}/100 \text{ nm}^2$. These defect densities are per QL. The corresponding mean distances between two interstitial defects and intercalated defects are ~ 20 and $\sim 8 \text{ nm}$, respectively. Although the mean

intercalated defect distance is smaller than the magnetic length $l_B \approx \sqrt{\hbar/eB}$ ($\sim 10 \text{ nm}$ at a magnetic field of 7 T) on such a surface, the discrete LLs were observed, as shown in Fig. 5(b). The dI/dV curves were obtained on the top of defect C (marked by an arrow in Fig. 5(a)) at 0 T (bottom) and 7 T (top) magnetic field. No impurity bound states of defect are observed at 0 T , while well-defined LLs can be resolved at 7 T . The observed LLs are insensitive to positions near to or far from the defects. With increasing defect density and when the mean interstitial defect distance is 7.5 nm , the LLs disappear. These results indicate the interstitial defect density plays a crucial role in the appearance of LLs. The electrons in surface states are strongly scattered by interstitial defects, not by intercalated defects. Thus, we concluded the surface states are localized to the first QL.²⁷

The interstitial Cu atoms can diffuse from one interstitial site to another by annealing at 480 K and can eventually move out of the QL. Defects B and C disappear, and the surface recovers to become a clean surface [Fig. 1(c)]. More importantly, the Dirac point of the annealed Cu-doped Bi_2Se_3 films shifts toward the E_F level and can recover to the Dirac point position of pure Bi_2Se_3 films. These results indicate that at a higher temperature the n -type doping nature of Cu atoms is not retained and the originally intercalated and interstitial Cu atoms might react with Bi and Se atoms to form a new phase, similar to the case of Cu-doped Bi_2Te_3 .^{28,29}

IV. CONCLUSIONS

The structural defects and electronic properties of the Cu-doped Bi_2Se_3 films have been studied. At room temperature and below, the Cu atoms can either intercalate into the van der Waals gaps, forming intercalated defects, or diffuse into the QL, developing interstitial defects. Both the intercalated and the interstitial Cu atoms lose one electron and thus act as donors. The discrete LLs are observed at a lower interstitial defect density. The structural information of the Cu-doped Bi_2Se_3 provided should be helpful for understanding the superconductivity in Cu-doped Bi_2Se_3 and for the investigation of other doped TIs.

ACKNOWLEDGMENTS

This work was supported by China's National Natural Science Foundation, the Ministry of Science and Technology of China, and the Chinese Academy of Sciences.

*xcma@aphy.iphy.ac.cn, qkxue@mail.tsinghua.edu.cn

¹M. Z. Hasan and C. L. Kane, *Rev. Mod. Phys.* **82**, 3045 (2010).

²X. L. Qi and S. C. Zhang, e-print [arXiv:1008.2026](https://arxiv.org/abs/1008.2026).

³H. J. Zhang, C. X. Liu, X. L. Qi, X. Dai, Z. Fang, and S. C. Zhang, *Nat. Phys.* **5**, 438 (2009).

⁴Y. Xia, D. Qian, D. Hsieh, L. Wray, A. Pal, H. Lin, A. Bansil, D. Grauer, Y. S. Hor, R. J. Cava, and M. Z. Hasan, *Nat. Phys.* **5**, 398 (2009).

⁵Y. L. Chen, J. G. Analytis, J. H. Chu, Z. K. Liu, S. K. Mo, X. L. Qi, H. J. Zhang, D. H. Lu, X. Dai, Z. Fang, S. C. Zhang, I. R. Fisher, Z. Hussain, and Z. X. Shen, *Science* **325**, 178 (2009).

⁶D. Hsieh, Y. Xia, D. Qian, L. Wray, F. Meier, J. H. Dil, J. Osterwalder, L. Patthey, A. V. Fedorov, H. Lin, A. Bansil, D. Grauer, Y. S. Hor, R. J. Cava, and M. Z. Hasan, *Phys. Rev. Lett.* **103**, 146401 (2009).

⁷Y. S. Hor, P. Roushan, H. Beidenkopf, J. Seo, D. Qu, J. G. Checkelsky, L. A. Wray, D. Hsieh, Y. Xia, S. Y. Xu, D. Qian,

- M. Z. Hasan, N. P. Ong, A. Yazdani, and R. J. Cava, *Phys. Rev. B* **81**, 195203 (2010).
- ⁸R. Yu, W. Zhang, H. J. Zhang, S. C. Zhang, X. Dai, and Z. Fang, *Science* **329**, 61 (2010).
- ⁹Y. S. Hor, A. J. Williams, J. G. Checkelsky, P. Roushan, J. Seo, Q. Xu, H. W. Zandbergen, A. Yazdani, N. P. Ong, and R. J. Cava, *Phys. Rev. Lett.* **104**, 057001 (2010).
- ¹⁰M. Kriener, K. Segawa, Z. Ren, S. Sasaki, and Y. Ando, *Phys. Rev. Lett.* **106**, 127004 (2011).
- ¹¹L. A. Fu and E. Berg, *Phys. Rev. Lett.* **105**, 097001 (2010).
- ¹²L. A. Wray, S.-Y. Xu, Y. Xia, Y. S. Hor, D. Qian, A. V. Fedorov, H. Lin, A. Bansil, R. J. Cava, and M. Z. Hasan, *Nat. Phys.* **6**, 855 (2010).
- ¹³P. Cheng, C. L. Song, T. Zhang, Y. Y. Zhang, Y. L. Wang, J. F. Jia, J. Wang, Y. Y. Wang, B. F. Zhu, X. Chen, X. C. Ma, K. He, L. L. Wang, X. Dai, Z. Fang, X. C. Xie, X. L. Qi, C. X. Liu, S. C. Zhang, and Q. K. Xue, *Phys. Rev. Lett.* **105**, 076801 (2010).
- ¹⁴C.-L. Song, Y.-L. Wang, Y.-P. Jiang, Y. Zhang, C.-Z. Chang, L. Wang, K. He, X. Chen, J.-F. Jia, Y. Wang, Z. Fang, X. Dai, X.-C. Xie, X.-L. Qi, S.-C. Zhang, Q.-K. Xue, and X. Ma, *Appl. Phys. Lett.* **97**, 143118 (2010).
- ¹⁵G. Kresse and J. Furthmüller, *Comput. Mater. Sci.* **6**, 15 (1996).
- ¹⁶J. P. Perdew, K. Burke, and M. Ernzerhof, *Phys. Rev. Lett.* **77**, 3865 (1996).
- ¹⁷P. E. Blöchl, *Phys. Rev. B* **50**, 17953 (1994).
- ¹⁸S. Nakajima, *J. Phys. Chem. Solids* **24**, 479 (1963).
- ¹⁹G. Henkelman, B. P. Uberuaga, and H. Jónsson, *J. Chem. Phys.* **113**, 9901 (2000).
- ²⁰S. K. Mishra, S. Satpathy, and O. Jepsen, *J. Phys.: Condens. Matter* **9**, 461 (1997).
- ²¹X. Chen, X. C. Ma, K. He, J. F. Jia, and Q. K. Xue, *Adv. Mater.* **23**, 1162 (2011).
- ²²H. Lind, S. Lidin, and U. Häussermann, *Phys. Rev. B* **72**, 184101 (2005).
- ²³R. O. Carlson, *J. Phys. Chem. Solids* **13**, 65 (1960).
- ²⁴A. Vaško, L. Tichý, J. Horák, and J. Weissenstein, *Appl. Phys.* **5**, 217 (1974).
- ²⁵Y. S. Hor, A. Richardella, P. Roushan, Y. Xia, J. G. Checkelsky, A. Yazdani, M. Z. Hasan, N. P. Ong, and R. J. Cava, *Phys. Rev. B* **79**, 195208 (2009).
- ²⁶T. Hanaguri, K. Igarashi, M. Kawamura, H. Takagi, and T. Sasagawa, *Phys. Rev. B* **82**, 081305 (2010).
- ²⁷W. Zhang, R. Yu, H. J. Zhang, X. Dai, and Z. Fang, *New J. Phys.* **12**, 065013 (2010).
- ²⁸J. Bludská, S. Karamazov, J. Navrátil, I. Jakubec, and J. Horák, *Solid State Ionics* **171**, 251 (2004).
- ²⁹J. Bludská, I. Jakubec, Č. Drašar, P. Lošt'ák, and J. Horák, *Philos. Mag.* **87**, 325 (2007).